Journal of Radiation and Nuclear Applications
An International Journal

http://dx.doi.org/10.18576/jrna/110205

Remote Sensing and Gamma Ray Spectrometry data combination for mapping alteration zones: A Case study from Saint Catherine Ring Complex, Southern Sinai, Egypt.

Remon N. Aziz[1,3], *Mohamed H. M. Yousef*[1], *Adel F. Khalel*[1], *S. M. M. Hanafy*[1], *Motoyuki Sato*[3], *El-Arabi H. Shendy*[2]

[1] Exploration Division, Nuclear Materials Authority, P.O. Box: 530, Maadi, Cairo, Egypt.
[2] Geology Department, Faculty of Science, Suez Canal University, Ismailia 41522, Egypt.
[3] Graduate School of Environmental Studies, Tohoku University, Sendai, Japan.

Received: 25 Dec. 2025, Revised: 15 Feb. 2026, Accepted: 1 Mar. 2026
Published online: 1 May. 2026

Abstract: Saint Catherine Ring Complex area in the Southern part of Sinai Peninsula is a very promising mineralization district located in Egypt. The current study provides two steps of approach from multisource datasets, including multispectral satellite data from ASTER, along with ground radiometric data and field verification, to identify hydrothermal alteration zones indicative of mineralization. Starting with ASTER data discrimination for lithological and alteration mapping, several image processing techniques of Remote sensing data, including False Color Composite (FCC), Principal Component Analysis (PCA), Independent Component Analysis (ICA), Minimum Noise Fraction (MNF), and band ratio (BR), Spectral Angle Mapper (SAM), and Constrained Energy Minimization (CEM). Multiple alteration zones of argillaceous, phyllic, and propylitic types were recognized, spatially correlated with alteration minerals including chlorite, calcite, kaolinite, sericite, and iron oxides. The generated mineralization potential map identifies five prospective sites for mineralization. Following a ground Gamma ray spectrometry survey at Wadi Um Qeisum area from multiple promising areas, the radiometric data were analyzed to delineate areas with the greatest potential for potassic alteration abundance by integrating potassium distribution, K/eTh ratio, eU-index, and F-parameter maps. The correlation between remote sensing and radiometry methods shows a highly effective scenario for mapping the hydrothermal radioactive materials related alteration zones.

Keywords: Remote Sensing, Gamma Ray Spectrometry, Saint Catherine Ring Complex, Hydrothermal Alteration, South Sinai

1 Introduction

The Catherine pluton is a central granite pluton within the Neoproterozoic Catherine Ring Complex, situated in the southern Sinai Peninsula, Egypt (Fig. (1). The composition includes syenogranite, alkali-feldspar granite (predominantly perthitic), and peralkaline granite. The two rock types are restricted to distinct levels of the pluton, thereby establishing its vertical zoning [1-3].

The hydrothermal alteration zones, along with the corresponding ore deposits and their structural controls, represent significant applications of remote sensing, particularly in regional mineral exploration [4].

The ASTER channels demonstrate superior continuity in the short-wave infrared spectrum relative to Landsat channels [5], hence improving their precision in the spectral identification of rocks and minerals [6]. As a result, they provide enhanced understanding of the geology and soils of the Earth's surface. ASTER data has demonstrated superiority over other sensors for lithological mapping [7-10].

The measurement of gamma ray energy and intensity enables the identification and spatial distribution of radiogenic materials, which may indicate lithological differences and structural aspects. Gamma-ray spectrometry in geophysics provides notable benefits, such as its non-destructive nature, elevated sensitivity, and ability to quickly cover large regions, especially in airborne surveys. Recent studies highlight its importance in delineating geotectonic environments, mapping alteration zones, and

*Corresponding author e-mail: remon_gph@yahoo.com

evaluating radiological risks across various geological contexts [11-13].

The heart of this study is a combination of remote sensing and ground geophysics methods to delineate the alteration and lithological mapping of a huge area, and then follow up with the ground gamma ray spectrometry method to detect these alteration zones and their relation with sulphide mineralization on the surface.

2 Geological Setting

We have two areas of study, one of which is Saint Catherine Ring Complex as a reconnaissance area, which we have studied using regional remote sensing data. We selected a small area for the ground geophysical survey to follow up the mineralization in the subsurface, which is, by the way, Wadi Um Qeisum area. So that we will briefly illustrate both of them geologically, structurally, and mineralogically.

The Saint Catherine Ring Complex comprises solely Late Neoproterozoic magmatic rocks, which are organized into two consecutively intruded series (Fig. 2) [14]. The oldest series includes I-type calc-alkaline quartz-diorites (e.g., Moneiga), quartz-monzonites, monzogranites, and the volcanic rocks of the Rutig Formation. Currently, none of these rocks has been accurately dated. However, our ongoing research on the predominant rock types, quartz-monzonites and monzogranites, suggests zircon ages ranging from 617 Ma to 603 Ma. The most recent series consists of A-type metaluminous and peralkaline high-silica granites, dated between 600 Ma and 590 Ma [15-16].

Wadi Um Qeisum constitutes a geological element of the Arabian-Nubian Shield (ANS), an important Precambrian terrain extending across northeastern Africa and the western Arabian Peninsula [17]. The shield is primarily composed of ancient igneous and metamorphic rocks, formed from the accretion of volcanic arcs and microcontinents during the late Neoproterozoic era [18-19].

An extensively modified region is located in the northwestern section of a significant quartz monzonite pluton. This region is delineated to the west by alkali feldspar granite and to the east by fresh quartz monzonite. The northeastern boundary of the modified region is delineated by quartz syenite rocks, which constitute a portion of a substantial ring dyke encircling the entire Saint Catherine area (Fig. 3) [20].

The drainage of the Saint Catherine area is regulated by extensive fracture systems. The various rock units are significantly influenced by multiple faults and joints exhibiting diverse trends and densities. The predominant fault trends are oriented north-south, northeast-southwest, northwest-southeast, and north-northwest-south-southeast. Less dominant trends are indicated by ENE-WSW and NNE-SSW orientations. These structures regulate a broadly distributed hydrographic system [21].

The Um Qeisum area is characterized by multiple structural lineaments oriented in various directions, with two primary fault sets constituting the principal structural components. The initial set consists of a series of long, parallel fault planes oriented in the NE-SW and NNE-SSW directions, aligned with the Gulf of Aqaba. The alternative set

runs parallel to the Gulf of Suez in a WNW-ESE orientation. A separate set of faults is oriented in the north-south direction, occurring with less frequency than the two primary orientations previously discussed (Fig. 3) [20].

The lineament extraction algorithm in PCI Geomatica software encompasses edge detection, thresholding, and curve extraction processes [22]. The directional analysis of the automatically extracted lineament maps (Fig. 4), which includes rose diagrams for both lineament directions and lengths, indicates the presence of two primary faulting trends: NE-SW and N-S, with NE-SW also identified as a minor faulting trend.

The mineralization in Wadi Um Qeisum is intricately linked to the tectonic evolution of the ANS, characterized by extensive faulting and shearing that facilitated the movement of hydrothermal fluids enriched with metals, resulting in the deposition of copper, gold, and other valuable minerals [23]. The geochemical characteristics and structural features of the region indicate the presence of typical orogenic gold and base metal mineralization, as commonly observed in the ANS [24].

3 Data and Methodology

3.1 Remote Sensing Data

The ASTER raw data is a raster file consisting of many stacked data points arranged in a grid covering approximately 4,500 km². A suitable image must be meticulously chosen to achieve optimal spectral response and precision. Geometrically and radiometrically calibrated ASTER Level_1B data for the study region, generated at the USGS Earth Resources Observation and Science (EROS) data center, were retrieved from the NASA Land Processes Distributed Active Archive Center (LPDAAC). Table 1 delineates the characteristics of the scene.

ASTER data consist of 14 channels that cover the Visible, Near Infrared (VNIR), Shortwave Infrared (SWIR), and Thermal Infrared (TIR) areas of the electromagnetic spectrum. The data demonstrate enhanced spatial, spectral, and radiometric resolutions relative to traditional Landsat data [26]. Each ASTER scene covers an area of 60 square kilometers by 60 square kilometers. The

VNIR bands have a spatial resolution of 15 m, the SWIR bands have a spatial resolution of 30 m, and the TIR bands have a spatial resolution of 90 m.

Table (1): The ASTER scene characteristics of the studied area.

Level	Scene No.	Date of acquisition	Time of acquisition	Cloud cover
AST_LIB	00305152001084518	May 15, 2001	08:45:18 am	0 %

3.1.1. ASTER Image preprocessing

a.Cross-talk correction against signal scattering issues in the SWIR sensor.

b.Atmospheric correction was eliminated using Dark

Object Subtraction (DOS)(FLAASH).

c.Pixel Resampling (The nine VNIR and SWIR 30m bands were stacked in one dataset).

d.The study area was extracted (subset) from the whole ASTER scene.

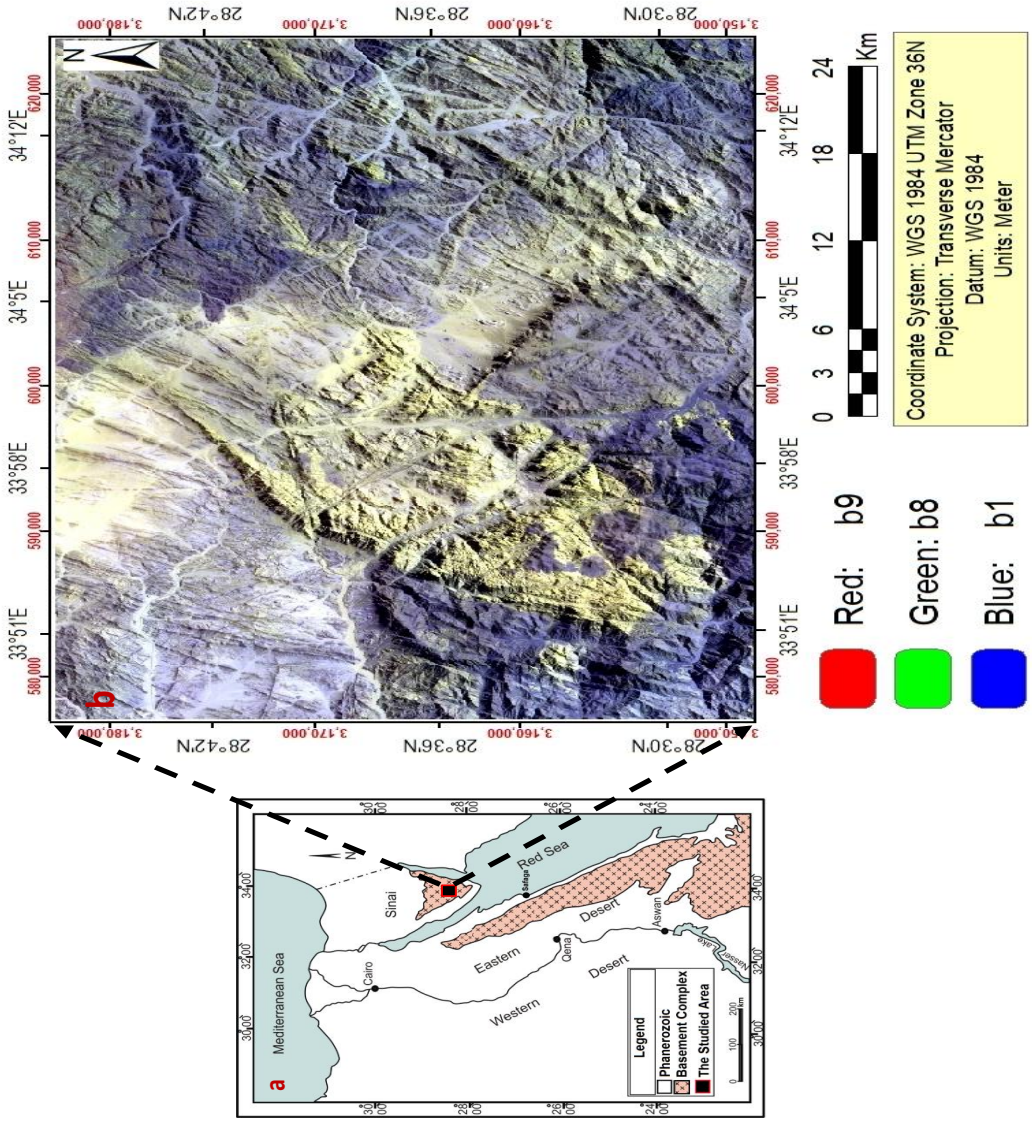

Fig. 1: (a) Location map, and (b) ASTER image of Saint Catherine area (bands 9, 8 & 1).

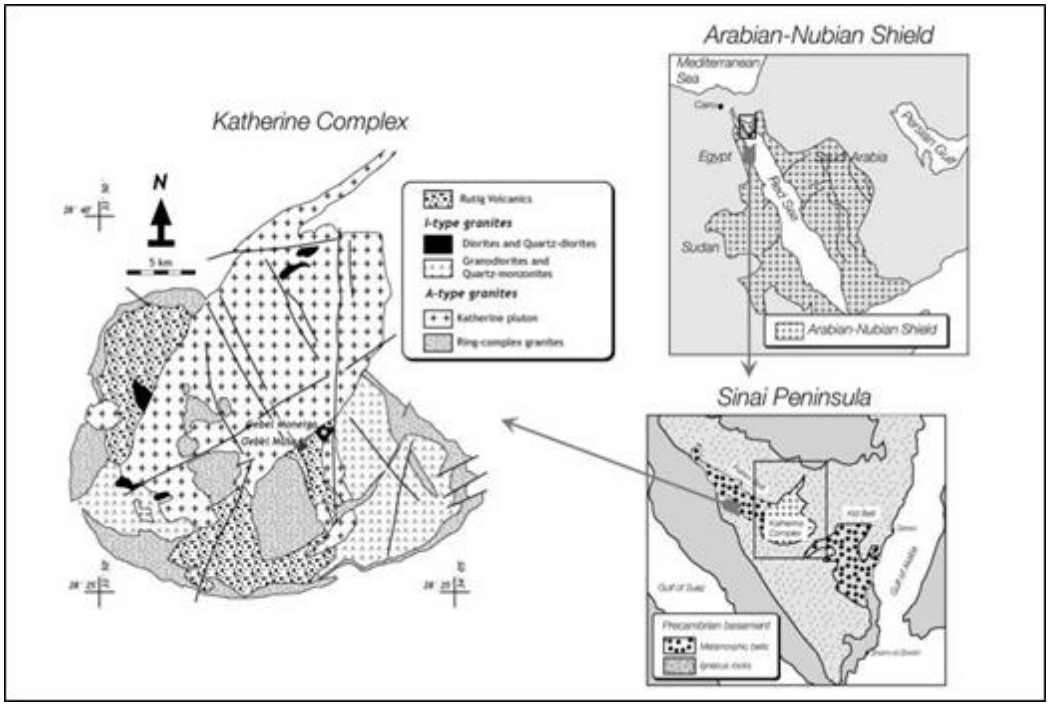

Fig. 2: Simplified geological sketch of the Catherine Complex and its position in the Arabian-Nubian Shield [25].

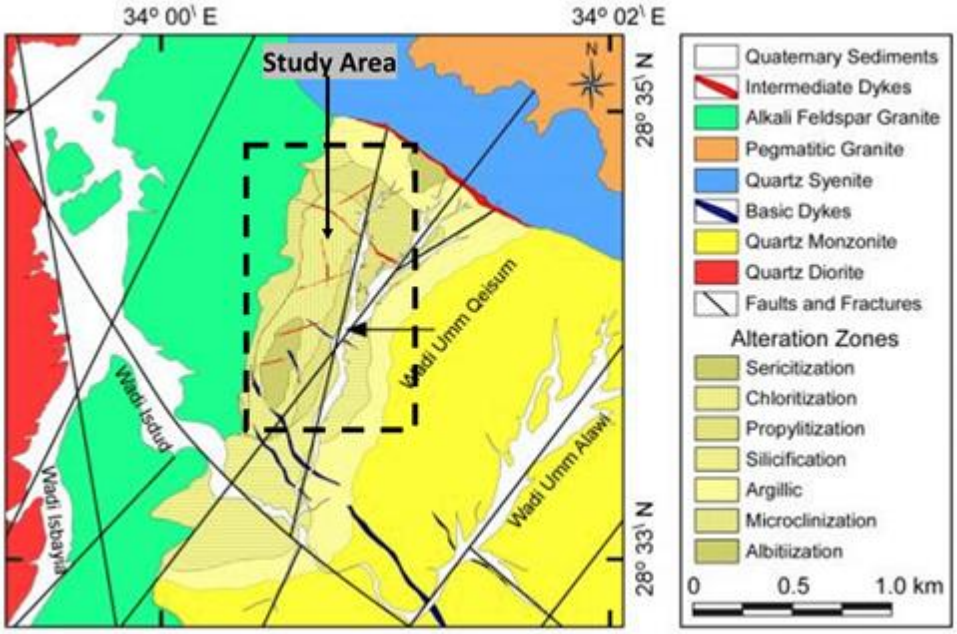

Fig.3: Geologic map of the study area showing the lithology and alteration zones [20].

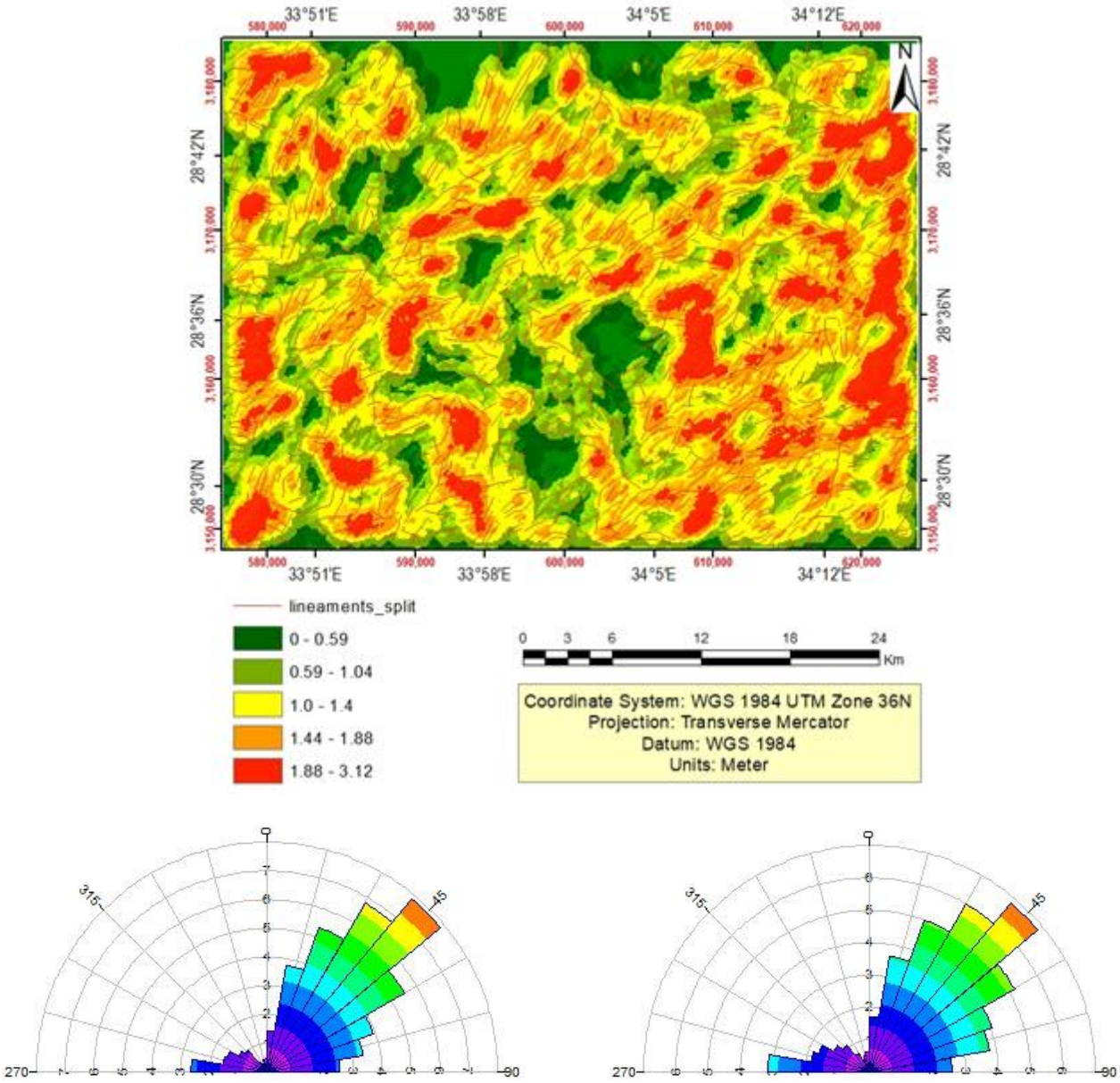

Fig.4: Lineaments extracted from the PCA map, with line density, and Rose diagrams show the trend analysis of the interpreted structures by number and length.

3.1.2 ASTER Image processing

This study employed an integrated remote sensing approach to map lithological units, extract lineaments, and identify alteration zones in the target area, utilizing ASTER satellite data processed with advanced software tools such as ENVI 5, Global Mapper 7, Ilwis 3.2, RockWork 18, PCI Geomatica, and ArcGIS v.10.8.

For alteration mapping with ASTER, spectral ratio indices (SRIs) like OHI, KLI, CLI, and b2/b1 identified OH-bearing minerals, kaolinite, and iron oxides. The Constrained Energy Minimization (CEM) technique mapped dominant altered minerals (e.g., kaolinite, illite, iron oxides) using VNIR-SWIR reflectance data, while Crosta PCA (FPCAs) analyzed specific bands (e.g., 4-6-7-9 for kaolinite) to delineate alteration minerals like alunite and montmorillonite.

For lithological mapping using ASTER, false color composite (FCC) images were generated by selecting optimal band triplets based on the Optimum Index Factor (OIF). The Color composite method assessed inter-band relationships, identifying low-correlation triplets, while the

OIF ranked combinations that maximized variance and minimized redundancy. RGB combinations were visually selected to enhance rock discrimination. Principal Component Analysis (PCA) was applied to VNIR-SWIR bands, capturing 99.9% of the data variance, with selected components used to highlight rock units and structures. The Minimum Noise Fraction (MNF) transform offers another sophisticated approach to handling the complexities of remote sensing data for applications like lithological mapping. Unlike PCA, which prioritizes variance, MNF focuses on separating the signal from the noise within the data.

Color ratio composites (CRC) further distinguish lithological units and alteration zones. Automatic lineament extraction involved generating shaded relief images from ASTER GeoDEM data in ArcGIS, producing lineament and density maps based on the number of lineaments per km².

3.2 Ground Gamma Ray Spectrometry

The survey data comprises total count (T.C) in uranium (Ur), equivalent uranium (eU in ppm), equivalent thorium (eTh in ppm), and potassium (K in %). The data were calibrated for background and stripping ratios to obtain the net concentrations of the three radioelements and the total gamma ray count.

A systematic ground Gamma Ray Spectrometry survey was executed in the research area, employing north-south oriented profiles organized in a grid configuration with 40m line spacing and 20m station spacing. The measurements were ultimately displayed as color radioactivity maps for TC, eU, eTh, K, eU/eTh, eU/K, uranium index, and F-parameter, along with a false-color composite image of eU, eTh, and K% utilizing the Geosoft program[27].

4 Results

4.1 Remote Sensing

ASTER SWIR imagery facilitates the identification of alteration zones linked to mineralization. Ore exploration target areas are determined based on the distribution of alteration zones and established mineral deposit models.

Significant alteration zones characterized by Phyllic, Argillaceous, and Potassic types typically indicate the presence of Porphyritic deposits. Hydroxide minerals are present in phylic (sericite and

montmorillonite), argillaceous (alunite and kaolinite), and propylitic (chlorite and calcite) environments, as well as in potassic (potassium feldspar and biotite) and oxidized minerals, particularly iron. Clay and silicate minerals are also found in phyllitic and argillaceous areas. Remote sensing techniques offer an effective approach for studying these minerals.

4.1.1 Alteration Mapping

- **Band Ratioing (BR)**

Band rationing is insensitive to intensity fluctuations; thus, materials with differing absolute reflectance but comparable relative reflectance over many bands will seem identical in the final image. A method for discovering brightness and ratio codes for Landsat TM and ASTER by identifying the spectral ratios that reflect the most distinctive spectral properties of a certain mineral [28].

This entails splitting the ratio values into deciles and awarding a value of nine to the highest decile. The target mineral or rock unit was demarcated by choosing the spectral band ratio with a high ratio code, especially 9 or 8, indicated in red, while the other two band ratios were assigned the lowest ratio codes of 0 or 1. Consequently, the dominating mineral or rock within the pixel will be represented in red, while other components will be assigned different hues [29].

The most appropriate band ratios that indicated the types of alterations were as follows:

1. Areas affected by ferrugenation alteration (Ferric iron oxides) took red shades in the 2/1, 4/3, 5/3 in R, G, B (BRC is 9, 6, 6) (Fig. 5).

2. Areas affected by kaolinization took the red and pink shades in the 7/5, 5/1, 6/1 in R, G, B color ratio composite (BRC is 8, 1, 1, respectively) (Fig. 6).
3. Areas affected by chloritization alteration took red and pink shades in the 6/2,8/6,3/1 in R, G, B color ratio composite (BRC is 9,1,0) (Fig. 7).
4. Illitization was highlighted with red shades in the 9/1, 7/5, 6/5 in R, G, B color ratio composite (BRC is 8, 3, 1) (Fig. 8).
5. Areas affected by sericitization alteration took ed shades in the 7/6, 9/7, 6/5 in R, G, B color ratio composite (BRC is 9,1,0) (Fig. 9).
6. Areas affected by silicification alteration took deep pink shades when applying the VNIR-SWIR band ratio 7/1,2/1,7/5 in R, G, B (BRC is 8,6,5) (Fig. 10).

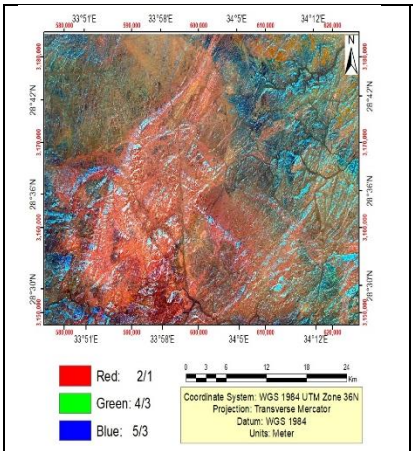

Fig. 5: Ferrugenation alteration zones (bright red) in Saint Catherine using the most discriminative BRCs of VNIR-SWIR bands.

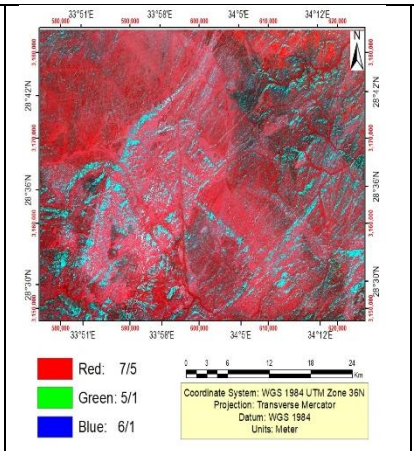

Fig.6: Kaolinization alteration zones (bright red) in Saint Catherine using the most discriminative BRCs of VNIR-SWIR bands.

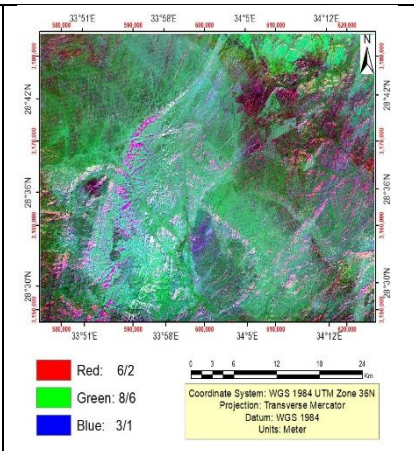

Fig.7: Chloritization alteration zones (bright red) in Saint Catherine area using the most discriminative BRCs of VNIR-SWIR bands.

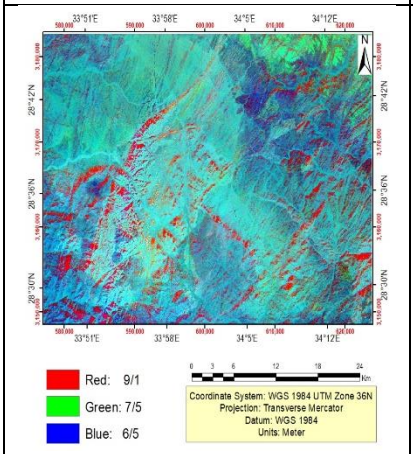

Fig.8: Illitization alteration zones (bright red) in Saint Catherine area using the most discriminative BRCs of VNIR-SWIR bands.

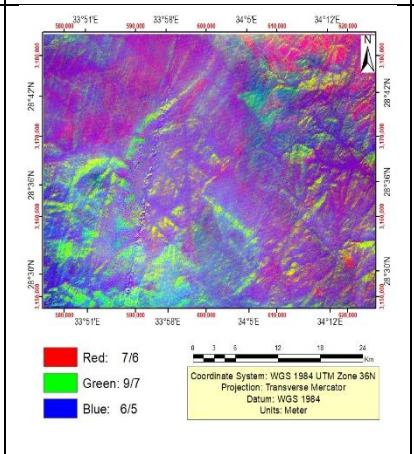

Fig.9: Sericitization alteration zones (bright red) in Saint Catherine area using the most discriminative BRCs of VNIR-SWIR bands.

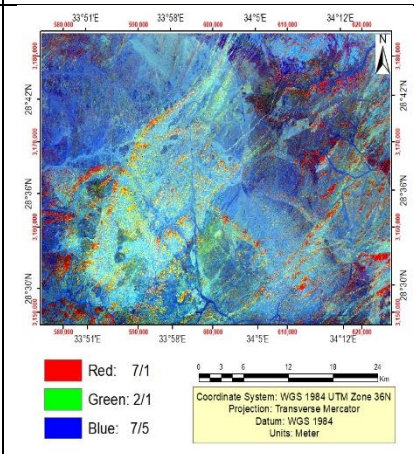

Fig.10: Silicification alteration zones (bright red) in Saint Catherine area using the most discriminative BRCs of VNIR-SWIR bands.

- **Crosta Technique (FBCS)**

This methodology was employed for mineral exploration using four and six selected bands of Landsat TM data [6, 30, 31,32 & 33] in addition to ASTER data [34].

To assess the input bands of the FPCS, the USGS library spectra of minerals were superimposed on the ASTER data band intervals within the VNIR-SWIR range (0.4 µm – 2.5 µm), as depicted in Figure 11. The examination of these charts enabled the identification of four bands for the FPCS (Crosta) Analysis, based on the spectral properties of the selected minerals within the VNIR-SWIR spectral ranges. The findings are encapsulated in Table 2. The alteration products discovered in the examined area through field and spectrometric analysis

include the following prevalent endmember alteration minerals: chlorite, kaolinite, illite, sericite, montmorillonite, and hematite in figures (12, 13, 14, 15, 16 & 17).

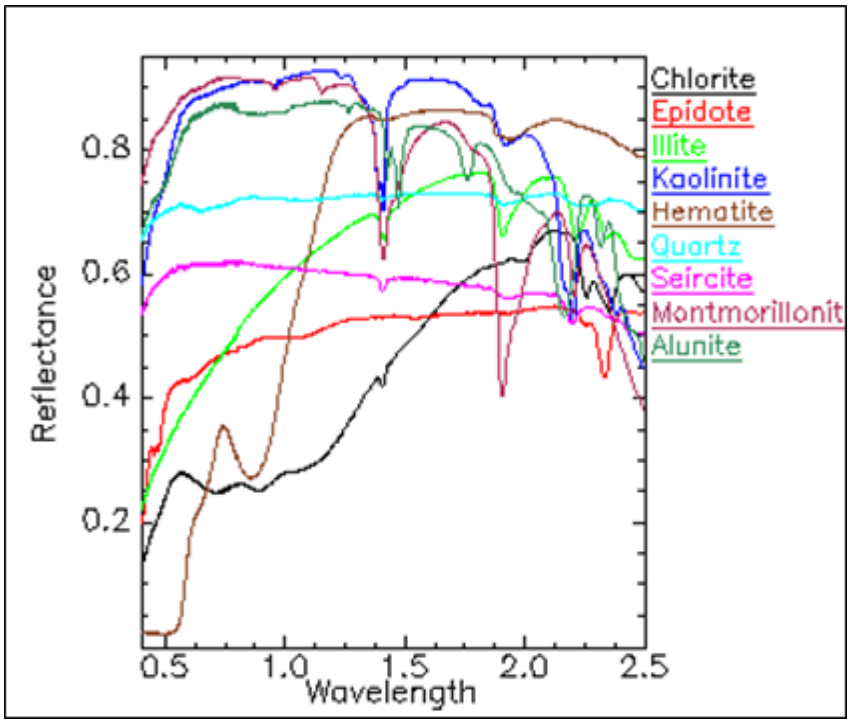

Fig. 11: The USGS library spectra of the studied minerals superimposed on ASTER data band intervals in the VNIR-SWIR region.

Table (2): Input bands for FPCS (Crosta) Analysis of the selected minerals.

Minerals	VNIR-SWIR (Reflectance)		Minerals	VNIR-SWIR (Reflectance)	
	High	Low		High	Low
Chlorite	Band 1 Band 5	Band 2 Band 8	**Hematite**	Band 2 Band 4	Band 3 Band 9
Kaolinite	Band 4 Band 7	Band 6 Band 9	**Montmorillonite**	Band 3 Band 7	Band 6 Band 9
Illite	Band 4 Band 7	Band 6 Band 8	**Seircite**	Band 4 Band 7	Band 6 Band 8
Epidote	Band 5 Band 6	Band 3 Band 8	**Alunite**	Band 3 Band 7	Band 5 Band 9
Quartz	Has no characteristic spectral features				

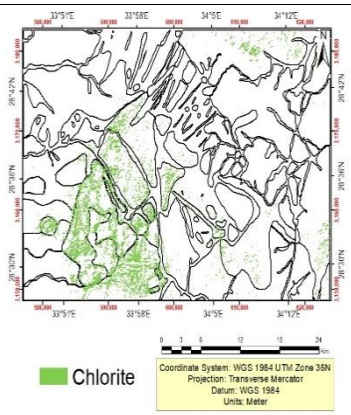

Fig.12: Resulted PC3 Chlorite image using FPCS (Crosta) technique for the input VNIR SWIR bands.

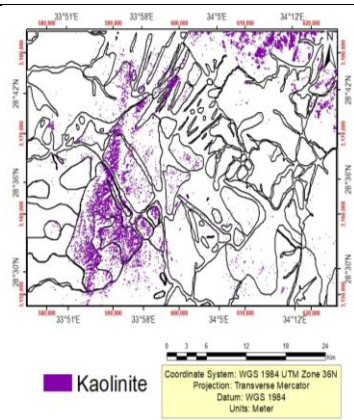

Fig.13: Resulted PC3 kaolinite image using FPCS (Crosta) technique for the input VNIR SWIR bands.

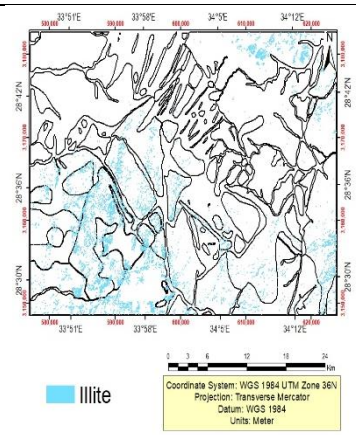

Fig.14: Resulted PC4 Illite image using FPCS (Crosta) technique for the input VNIR SWIR bands.

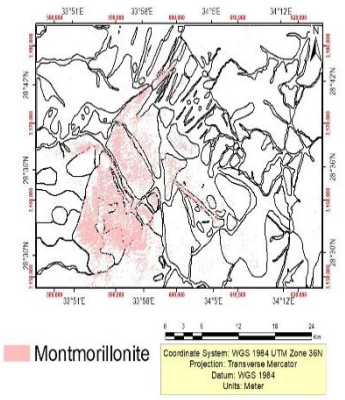

Fig.15: Resulted PC3 montmorillonite image using FPCS (Crosta) technique for the input VNIR SWIR bands.

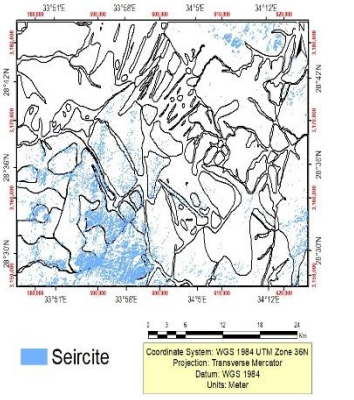

Fig.16: Resulted PC4 sericite image using FPCS (Crosta) technique for the input VNIR SWIR bands.

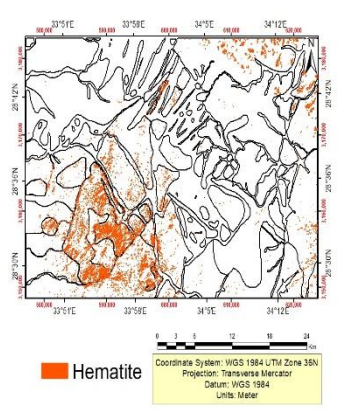

Fig.17: Resulted PC4 Hematite image using FPCS (Crosta) technique for the input VNIR SWIR bands.

- **Constrained Energy Minimization (CEM)**

This approach is akin to matched filtering, as it requires the recognition of the target's spectral signature for detection solely. This algorithm operates as automated gain control by optimizing the response of a designated spectrum while attenuating the response of the unidentified background signature [35,36].

The ASTER resampled Jet Propulsion Laboratory (JPL) spectral library, which encompasses the VNIR-SWIR spectral region (Version 1.2, http://speclib.jpl.nasa.gov), has been utilized to identify the primary endmember alteration minerals: chlorite, kaolinite, illite, sericite, montmorillonite, and hematite (Fig. 18).

The resulting image (Fig. 19) shows the chlorite mineralization that exceeds the threshold value as green colored areas. Thresholding DN value for kaolinite (= 190), the resultant image represents kaolinite mineral as magenta (Fig. 20). Thresholding DN value for illite (= 189), the resultant image represents Illite mineral as blue (Fig. 21). Thresholding DN value for sericite (= 191), the resultant image represents sericite mineral as cyan (Fig. 22). Thresholding DN value for montmorillonite (= 197), the resultant image represents montmorillonite mineral as violet (Fig. 23). Thresholding DN value for hematite (= 205), the resultant image represents hematite mineral as red (Fig. 24).

The CEM method effectively identified alteration minerals in the VNIR-SWIR spectral regions, demonstrating varying levels of accuracy. The types of alterations and localities identified through CEM correspond to hydrothermally altered rocks previously enhanced by the Crosta-Moore technique (FPCA) and band rationing (BR).

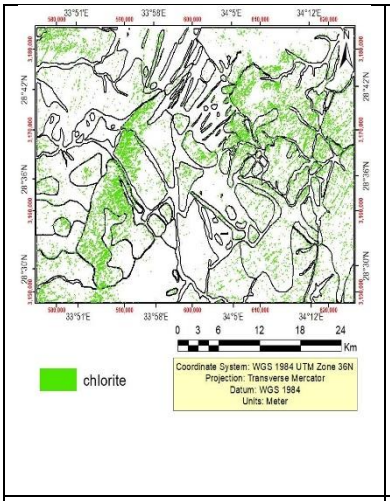

Fig.19: Separated CEM classification endmember (Chlorite) using VNIR-SWIR stack and the JPL ASTER resampled spectral library.

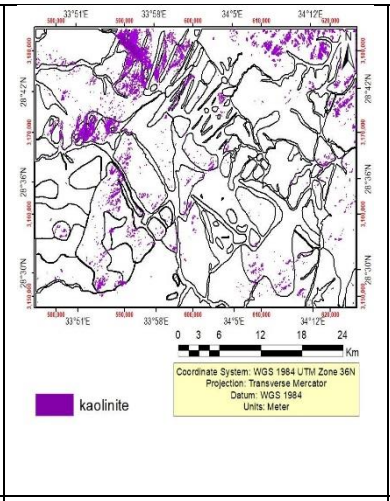

Fig.20: Separated CEM classification endmember (kaolinite) using VNIR-SWIR stack and the JPL ASTER resampled spectral library.

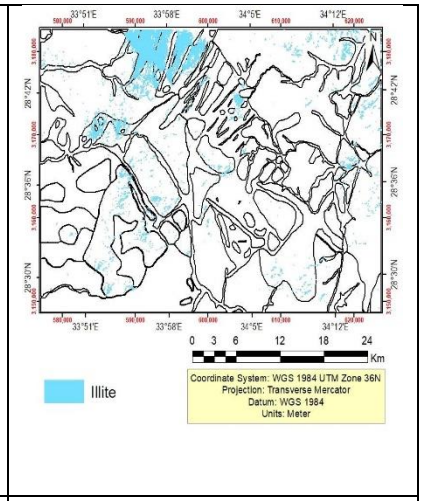

Fig.21: Separated CEM classification endmember (Illite) using VNIR-SWIR stack and the JPL ASTER resampled spectral library.

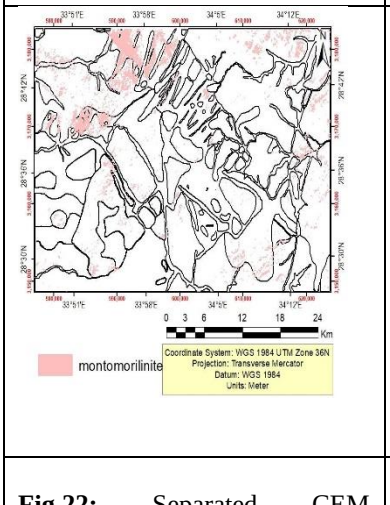

Fig.22: Separated CEM classification endmember (Montmorillonite) using VNIR-SWIR stack and the JPL ASTER resampled spectral library.

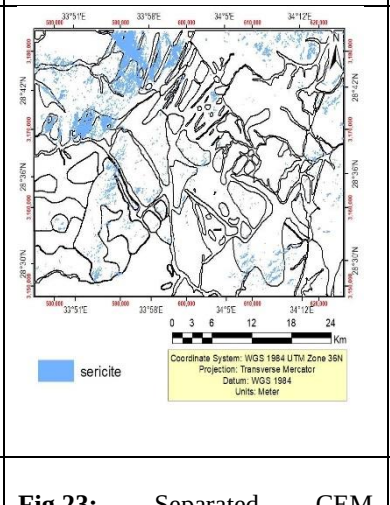

Fig.23: Separated CEM classification endmember (Sericite) using VNIR-SWIR stack and the JPL ASTER resampled spectral library.

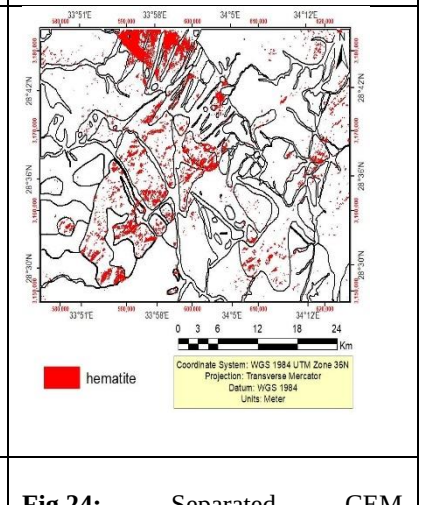

Fig.24: Separated CEM classification endmember (Hematite) using VNIR-SWIR stack and the JPL ASTER resampled spectral library.

4.1.2. lithological mapping

False color composite (FCC)

The optimum index factor (OIF) is a statistical measure employed to assess all potential three-band combinations, such as RGB [37,38]. The OIF values are calculated to determine the optimal band combinations, and the bands are prioritized according to the information included in each combination. The capacity for RGB visualization is contingent upon the overall variance and correlation among various bands [39,40]. Bands exhibiting elevated OIF values were chosen for enhanced lithological differentiation, as they encompass bands characterized by maximal variance and minimal redundancy [39,40]. Table 3 enumerates the 10 foremost band combinations. Upon visual examination of the optimal band triplet options derived from OIF methodology, RGB pictures 9, 8, and 1 were chosen for enhanced lithological differentiation of the exposed rocks in the region (Fig. 25).

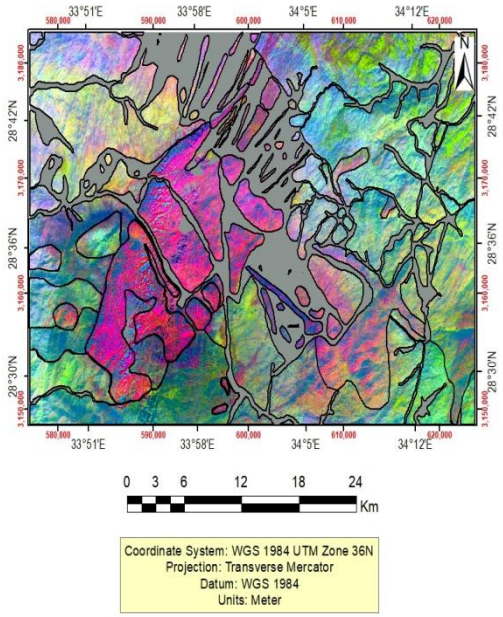

Fig. 27: Supervised Classification using Minimum noise fraction by Spectral Library from ASTER Image at Saint Catherine area.

4.2 Gamma Ray Spectrometry

- **Radioelement concentration distribution maps**

In general, the four radiometric maps (Fig. 28a, b, c, and d) show different levels over the surveyed area, reflecting a contrast in radioelement contents for the exposed various rock types. This variability reflects a heterogeneous distribution of radioactive elements, which may correspond to structural features such as faults or zones of alteration. Generally, TC, eU, eTh, and K% maps (Fig. 28a, b, c, and d), the surveyed area displays a wide range of radioactivity, ranging from approximately 11.6 to 120.4 Ur, 0.2-58.4 ppm, 2.0-103.0 ppm, and 1.2-7.9 %, respectively.

High values are predominantly located in the northwestern and central-western regions of the map. The zones are linked to alkali feldspar granites and altered rock units, indicating possible hydrothermal alteration, mineralized veins, or intrusions enriched in radioactive elements. Moderate values are predominantly found in the central and northeastern regions, likely associated with partially weathered or altered felsic rocks.

Low values predominate in the southeastern and southern regions of the map. Lower readings may suggest the presence of structural depressions or drainage zones, where erosion or leaching has diminished the concentration of radioactive elements. A northwest-southeast trending pattern of alternating high and low radioelement zones indicates the potential influence of structural lineaments or faults on radioelement distribution. Elongated anomalies, particularly in the central-western region, may indicate the presence of dikes or vein systems enriched in uranium and thorium. Irregular, spot-like anomalies may signify localized mineralized pockets or alteration halos, potentially associated with intrusive bodies.

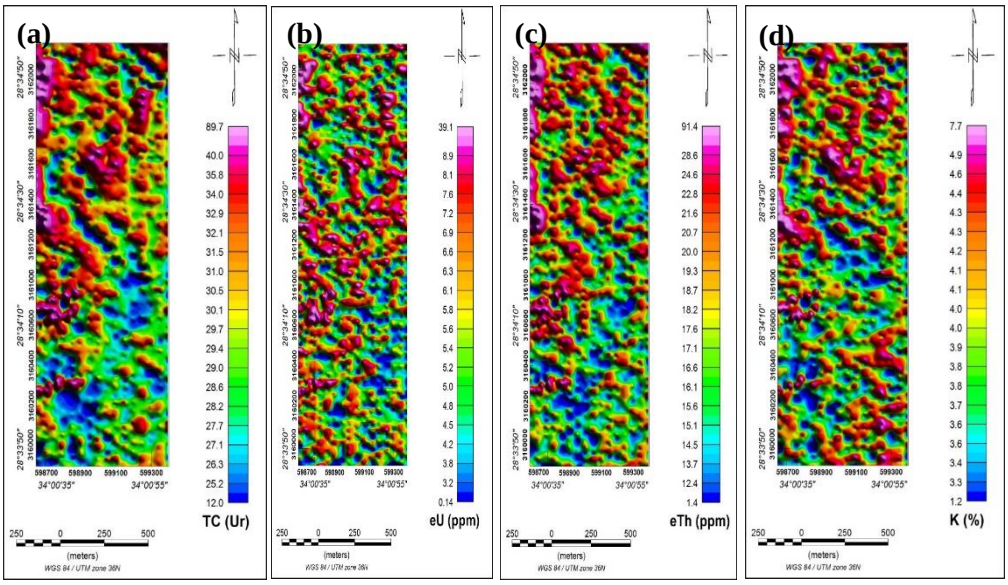

Fig. 28: (a) Total count (TC) map in Ur, (b) equivalent uranium (eU) map in ppm, (c) equivalent thorium (eTh) map in ppm, and (d) potassium (K) map in % map, Wadi Um Qeisum, Southern Sinai, Egypt.

- **The ratio and ternary maps**

The eU/eTh and eU/K ratios for the study area were illustrated using color ratio maps (Figs. 29. a and 29 b). In natural geochemical equilibrium, the typical background values for the eU/eTh ratio are approximately 0.2 to 0.6, indicating the relative immobility of thorium compared to uranium. Anomalous values typically commence at 0.7, with values surpassing 1.0-1.2 signifying substantial uranium enrichment, frequently resulting from mobilization and redeposition in oxidizing environments [49-51].

Figure 29. a presents the eU/eTh ratio map, with contour lines indicating zones exceeding 0.5. The eU/K ratio, indicating the relative abundance of uranium to potassium, typically exhibits background values ranging from 0.5 to 1.0. Anomalous zones are identified when the ratio surpasses 1.5, with values exceeding 2.0 deemed highly anomalous, typically indicating potassium depletion (e.g., due to sericitization) or uranium enrichment via hydrothermal solutions (52, 53, 54 & 55). The contour lines in the eU/K ratio map delineate areas exceeding 2.0 (Fig. 29.b).

Reddish areas denote potassium-rich zones, bluish and greenish tones represent uranium- and thorium-enriched regions, white indicates balanced high concentrations, and dark areas signify low radioelement content (Fig. 30.a).

Composite maps for U, Th, and K (Figs. 30.b, 30.c, and 30.d) improve comprehension of elemental distribution and facilitate the identification of geochemical anomalies. The uranium map (Fig. 30.b) illustrates elevated uranium concentrations and regions exhibiting high eU/eTh and eU/K ratios, potentially associated with uranium-rich lithologies, alteration zones, or rare earth element (REE) potential. The thorium map (Fig. 30.c) illustrates zones enriched in thorium, correlated with remaining minerals such as monazite and xenotime, which are prevalent hosts for rare earth elements. The potassium map (Fig. 30.d) illustrates areas of elevated K content and potassic alteration, frequently associated with felsic intrusions or pegmatites. These maps offer essential insights into potential rare earth element mineralization zones by highlighting overlapping anomalies of uranium, thorium, and potassium.

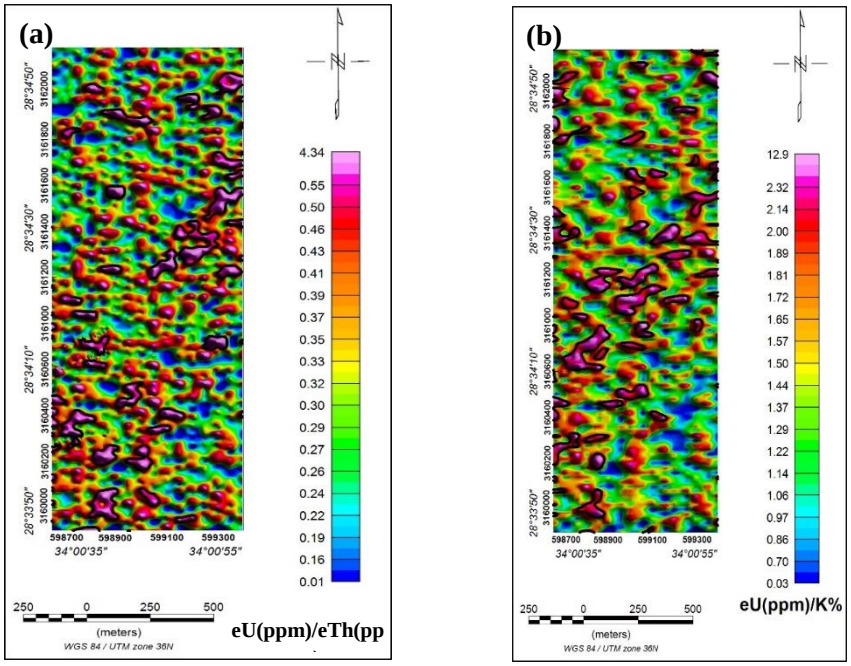

Fig. 29: (a) eU/eTh map, (b) eU/K% map, (c) uranium index map.

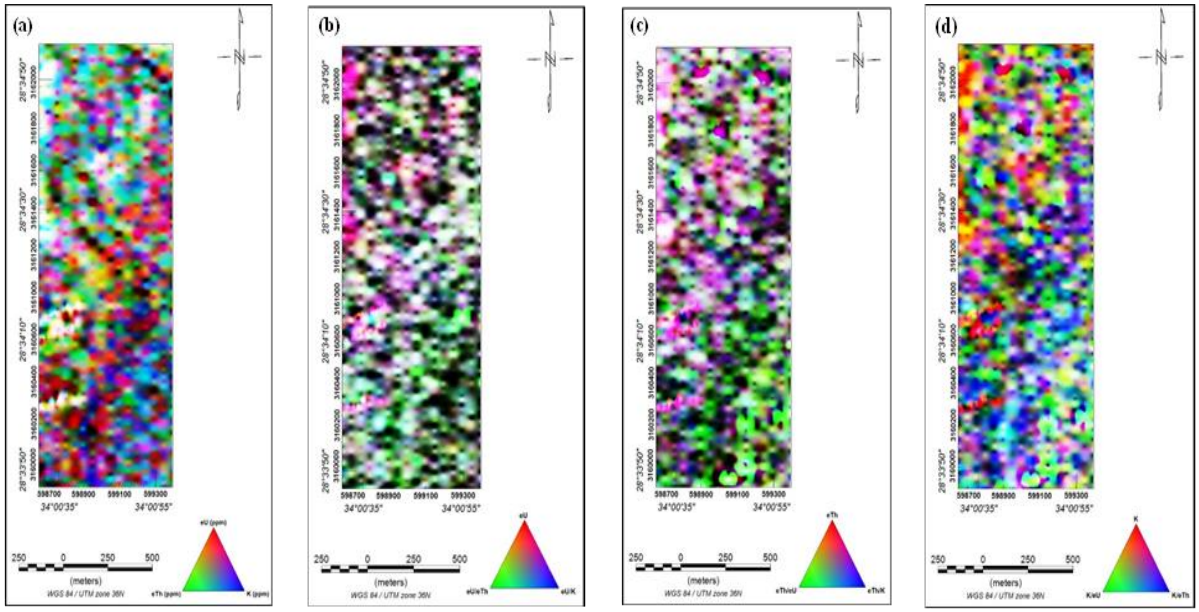

Fig. 30: False-color composite images of (a) the three radioelements, (b) uranium, (c) thorium, and (d) potassium, Wadi Um Qeisum, Southern Sinai, Egypt.

- **U Index and F-parameter maps**

The U Favorability Index (U-Index), introduced by [56], is a ratio designed to assess the relative enrichment of uranium (eU) compared to thorium (eTh) and potassium (K) in rocks. It is expressed as:

U-index = (eTh*K)/eU ……. (1)

The U-Index delineates areas of uranium enrichment relative to the geochemically stable elements thorium and potassium. Elevated values generally indicate secondary uranium mobilization by hydrothermal processes, weathering, or redox reactions, while diminished values suggest equilibrium or depletion [52, 55 & 57].

This method is particularly effective for identifying alteration zones and potential mineralization in sedimentary, volcanic, and granitic terrains. Background values typically approximate 1, whereas values exceeding 1.5-2 are deemed anomalous, and those surpassing 3-4 may suggest significant uranium mobilization [51, 52& 55). This study contoured U-Index values exceeding 2 (Fig. 31.a) to identify areas of intense alteration and mineralization.

F = K (eU/eTh)……. (2)

Where: eU = equivalent uranium concentration (ppm), eTh = equivalent thorium concentration (ppm), K = potassium concentration (%).

The F-parameter in unmodified rocks typically ranges from 1.2 to 1.3, signifying equilibrium distributions of elements in dominant rock-forming minerals. Rocks that have undergone hydrothermal alteration or weathering frequently have markedly elevated F-values, usually between 2 and 5, and occasionally up to 10. This phenomenon is attributed to the selective mobilization and enrichment of uranium, coupled with the depletion of thorium and potassium during alteration processes [58-59]. This variance supports the utilization of the F-parameter in geological and mineral exploration, particularly in detecting alteration zones and uranium deposits. Figure 31.b depicts the F-parameter map of the research area, emphasizing the regions of significant modification (exceeding 2.0).

5 Discussion

Using all the above techniques for lithological mapping, like a principal component analysis image (PC3, PC2, PC1, in RBG), Spectral angle mapping, and Minimum Noise Fraction for spectral library from ASTER image. These various images were used for the geological and structural mapping of the area (Fig. 32).

The current study suggests some new localities for Uranium exploration that have similar conditions as the explored sites at Saint Catherine area (Fig. 33). The conversion of VNIR-SWIR identified the primary endmember alteration minerals: chlorite, kaolinite, illite, sericite, montmorillonite, and hematite. Their locations are illustrated in Figure 33

The final map indicates several promising areas characterized by a higher anomaly of alteration minerals, necessitating further exploration.

A map was generated to integrate the gamma-ray spectrometric data, featuring contour lines representing the highest values for eU/eTh, eU/K, uranium-index, and F-parameter, as previously detailed. Then a map was created based on the aggregation of these contours, highlighting the highest potential zones for mineral exploration, particularly for rare earth elements (REE) (Fig. 34).

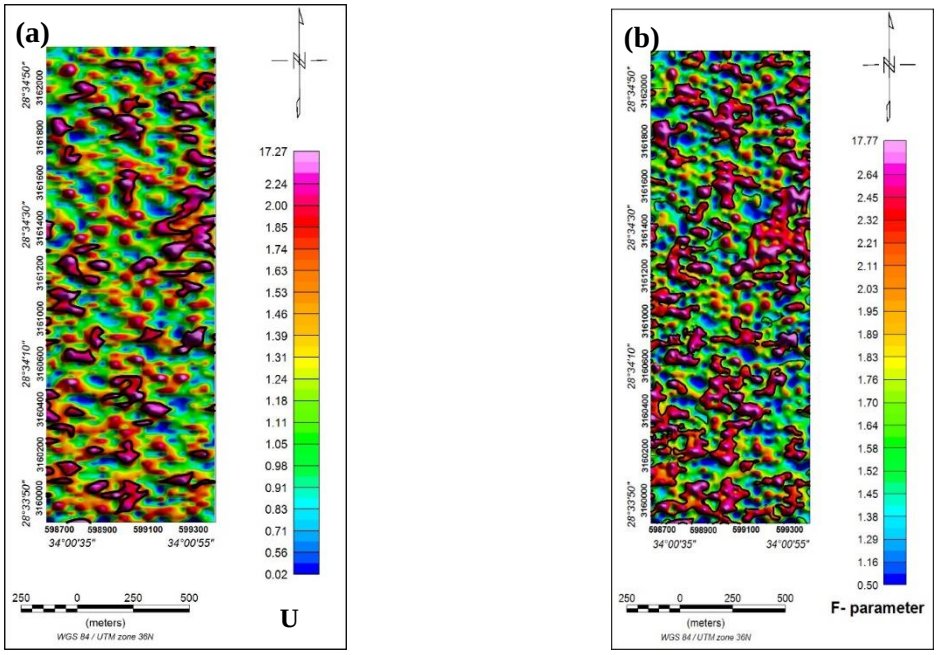

Fig. 31: (a) uranium index map, and (b) F-parameter map, Wadi Um Qeisum, Southern Sinai, Egypt.

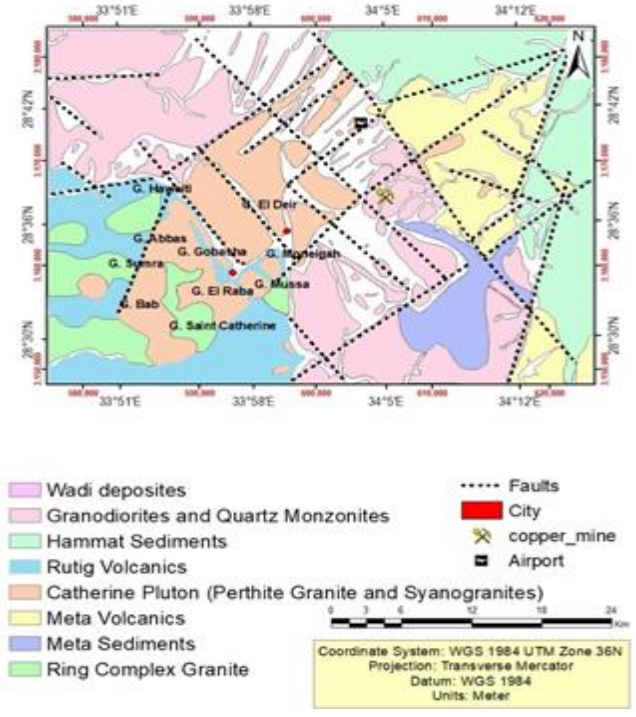

Fig. 32: Interpreted geologic map of Saint Catherine area.

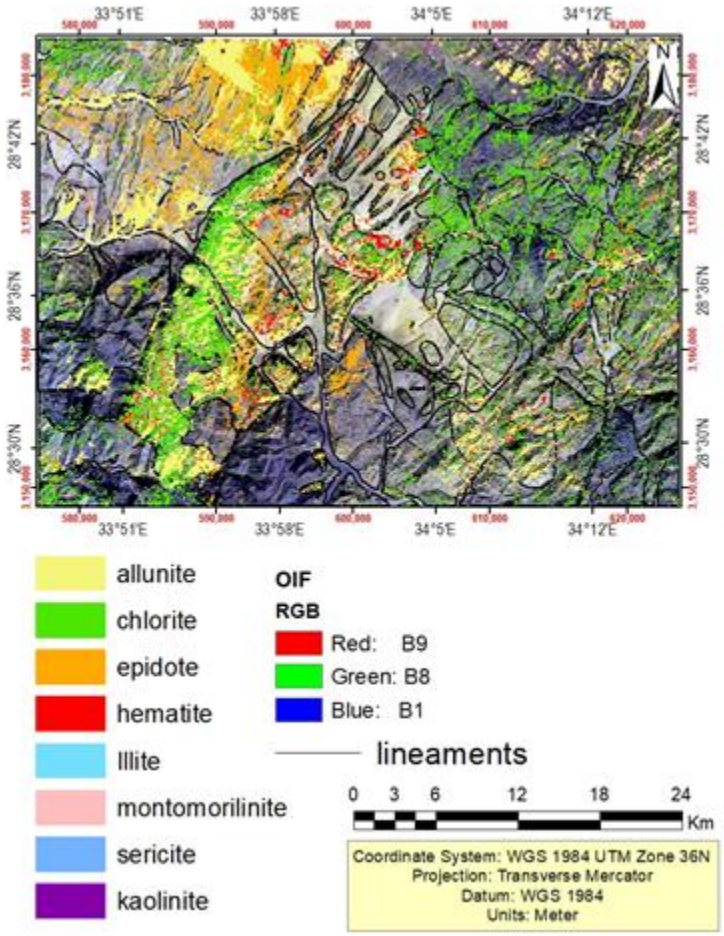

Fig. 33: CEM classified endmembers and lineaments overlying high-ranked OIF as RGB.

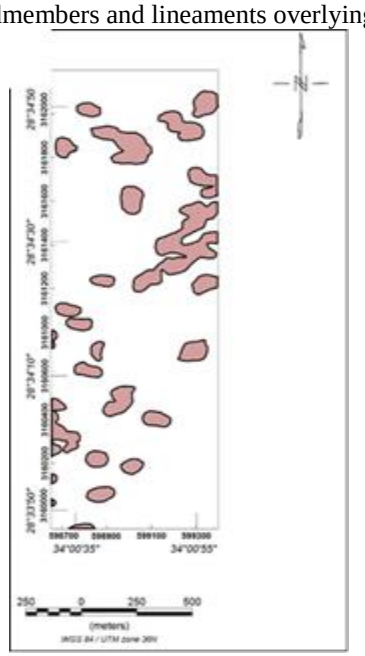

Fig. 34: high anomalous zones, Wadi Um Qeisum, Southern Sinai, Egypt.

6 Conclusions

The ASTER image spectrometry data in the VNIR and SWIR spectral regions, analyzed through various image classification methods, indicate specific spectral characteristics for the Saint Catherine area.

In the Saint Catherine area, various processing and analysis techniques were utilized on ASTER data to map the prevalent alteration minerals. The techniques employed comprised Band Ratio code, Feature Oriented Principal Component Selection (FPCS) as proposed by Crosta and Moore, and Constrained Energy Minimization (CEM). All these techniques were effective in detecting the alteration minerals of the Endmember.

Lithological studies employed multiple techniques, including ASTER bands 9, 8, and 1, which produced the most effective false color composite image, achieving the highest optimum index factor (OIF = 76.68). Additionally, Principal Component Analysis (PCA), Spectral Angle Mapper, and Minimum Noise Fraction (MNF) were utilized for the spectral library derived from the image. These techniques were employed to develop a new lithological and structural map for the Saint Catherine area.

Structural lineaments are extracted automatically through the application of Principal Component Analysis (PCA) mapping. The results obtained from both techniques demonstrate a strong correlation. The directional analysis of the automatically extracted lineament maps, including rose diagrams and histogram frequency distributions of lineament directions and lengths, indicated that the predominant trends in the area are NW-SE, NNW-SSE, E-W, and N-S, in descending order, with NE-SW identified as a minor faulting trend.

Gamma-ray spectrometric data offered further understanding of the distribution of radioactive elements. Maps depicting equivalent uranium (eU), equivalent thorium (eTh), and potassium (K), as well as their ratios including eU/eTh, eU/K, uranium favorability index (U-Index), and the F-parameter, facilitated the identification of hydrothermal alteration zones and potential enrichment of rare earth elements (REE). The spatial correlation of these radiometric anomalies with pegmatite bodies and altered quartz monzonite underscores their importance as exploration targets.

References

[1] Jahn, B.-M., Wu, F.Y., Chen, B., 2000: Granitoids of the Central Asian Orogenic Belt and continental growth in the Phanerozoic. Trans. R. Soc. Edinb. Earth Sci. 91, 181–193.

[2] Jahn, B.-M., Capdevila, R., Liu, D., Vernov, A., Badarch, G., 2004: Sources of Phanerozoic granitoids in the transect Bayanhongor-Ulan Baator, Mongolia: geochemical and Nd isotopic evidence, and implications of Phanerozoic crustal growth. J. Asian Earth Sci. 23, 629–653

[3] SA Taalab, M Al Meshari, Y Alzamil, Ahmad Abanomy, Amjad R Alyahyawi, Waheed H Mohamed, Atef El-Taher., 2023, Radiological and ecological hazards evaluation of episyenite used as building materials. Journal of Radioanalytical and Nuclear Chemistry, 332 (4)

[4] Ali, H. F., Abo El Ata, A. S. A., Youssef, M. A. S., Salem, S. M., & Ghoneim, S. M. A newly-developed multi-algorithm integration technique for mapping the potentially mineralized alteration zones. Egypt. J. Remote Sens. Space Sci. 26(3), 691–711 (2023).

[5] Abdel Gawad, AE., MA Ali, MM Ghoneim, A. El-Taher.,2023, Natural radioactivity and mineral chemistry aspects of rare metal mineralization associated with mylonite at Wadi Sikait, South Eastern Desert, Egypt. International Journal of Environmental Analytical Chemistry 103 (10), 2300-2317.

[6] Crosta A P, McM Moore J., 1989: Enhancement of Landsat thematic mapper imagery for residual soil mapping in SW Minais Gerrain. In: Proceedings of the 7th (ERIM) Thematic Conference: Remote Sensing for Exploration Geology Calgary, 1989: 1173–1187.

[7] Zhang, X. and Pazner, M., 2007: Comparison of Lithologic Mapping with ASTER, Hyperion and ETM Data in the southeastern Chocolate Mountains, USA. Photogrammetric Engineering and Remote Sensing, 73(5): 555-561.

[8] Gad, S., and KUSKY, T., 2006: Lithological mapping in the Eastern Desert of Egypt, the Barramiya area, using Landsat thematic mapper (TM). Journal of African Earth Sciences, 44(2): 196-202.

[9] Gad, S. and Kusky, T., 2007: ASTER spectral rationing for lithological mapping in the Arabian–Nubian shield, the Neoproterozoic Wadi Kid area, Sinai, Egypt. Gondwana Research, 11(3): 326-335.

[10] Raharimahefa, T. and Kusky, T.M., 2009: Structural and remote sensing analysis of the Betsimisaraka Suture in northeastern Madagascar. Gondwana Research, 15(1): 14-27.

[11] Ghoneim, Mohamed M., Elena G. Panova, Ahmed E. Abdel Gawad, Hamdy A. Awad, Hesham M.H. Zakaly, Atef El-Taher., 2021 Analytical methodology for geochemical features and radioactive elements for intrusive rocks in El Sela area, Eastern Desert, Egypt. International journal of environmental analytical chemistry. 103 (6), 1272-1291.

[12] Atef El-Taher, A Mohamed, L Yehia, G Salaheldin, R Elsman, HA Khamis, AA Ahmed 2022 Spatial Distributions and Risk Assessment of the Natural Radionuclides in the Granitic Rocks from Gabal Gattar

II, Eastern Desert, Egypt. Radiochemistry 64 (6), 783-792.

[13] Abd El-Rahman, M. A., Mohamed, H. A., & Hassan, A. M. 2024: Radiological Assessment of Rare Metal-Bearing Granites Using Gamma-Ray Spectrometry. Journal of Radioanalytical and Nuclear Chemistry. https://doi.org/10.1007/s10967-024-09852-5.

[14] Azer, M.K., 2007: The petrogenesis of late Precambrian felsic alkaline magmatism in South Sinai, Egypt. Acta Geologica Polonica, 56, 463-484.

[15] Ghoneim, M.F.; Lebda, E.M. and Abu Anbar, M.M., 1999: Further geochemical and mineralogical discrimination between granitic rocks of Eastern Desert of Egypt. (GAW 4) Int. Conf. On the Geology of the Arab World, Cairo Univ., Cairo 21-25 Feb. 1998, 1, 266286.

[16] Katzir, R. (2007): Structurally-defined alternatives. Linguist and Philos 30, 669–690. https://doi.org/10.1007/s10988-008-9029-y.

[17] Stern, R.J. (1994): Arc-Assembly and Continental Collision in the Neoproterozoic African Orogen: Implications for the Consolidation of Gondwanaland. Annual Review of Earth and Planetary Sciences, 22, 319-351.
https;//doi.org/10.1146/annurev.earth.22.1.319.

[18] Johnson PR, Andresen A, Collins AS, Fowler AR, Fritz H, Ghebreab W, Kusky T, Stern RJ (2011): Late Cryogenian-Ediacaran history of the Arabian-Nubian Shield: a review of depositional, plutonic, structural, and tectonic events in the closing stages of the northern East African Orogen. J Afr Earth Sci 61:167–232.

[19] Abd El-Wahed, M., Hamimi, Z. (2021): The Egyptian Nubian Shield Within the Frame of the Arabian–Nubian Shield. In: Hamimi, Z., Arai, S., Fowler, AR., El-Bialy, M.Z. (eds) The Geology of the Egyptian Nubian Shield. Regional Geology Reviews. Springer, Cham. https://doi.org/10.1007/978-3-030-49771-2_2.

[20] Rashed, Mohamed A., and El-Arabi H. Shendi. 2022: "Construction of a 3D Conceptual Model of Subsurface Sulfide Mineralizations Using Integrated Geophysical Survey in Saint Catherine, South Sinai, Egypt". Journal of Scientific Research and Reports 28 (1):23-34. https://doi.org/10.9734/jsrr/2022/v28i130484.

[21] El Fouly A. A., (2000): Faults and Fractures Intersections Delineation as a Tool for Groundwater Detection Using Remote Sensing and Ground Penetrating Radar Techniques at Saint Catherine area, Southern Sinai, Egypt. ICEHM2000, Cairo o University, Egypt, September, pages 293- 310.

[22] Abdelmohsen, M., Elhaddad, MA., El-Taher, A., 2025 Natural radioactivity levels and radiation hazards in some magmatic rocks from the eastern and western deserts. Euro-Mediterranean Journal for Environmental Integration 10 (3), 1215-1242

[23] Helmy, H. M., & Kaindl, R. 2002: Gold mineralization in the Arabian-Nubian Shield: A case study from Wadi Um Qeisum, South Sinai, Egypt. Mineralogy and Petrology, 74(1-2), 91-108.

[24] Abu El-Ela, F., & Mohamed, F. H. 2015: Rare earth element potential in the hydrothermal alteration zones of Wadi Um Qeisum, Sinai Peninsula, Egypt. Ore Geology Reviews, 65, 613-629.

[25] Bea, F., Montero, P., Gonzalez Lodeiro, F., Talavera, C., 2007: Zircon inheritance reveals exceptionally fast crustal magma generation processes in Central Iberia during the Cambro-Ordovician. Journal of Petrology 48, 2327–2339.

[26] Abrams, M. and Hook, S., 2001: ASTER user handbook (version 2). Jet Propulsion Laboratory, Pasadena, CA-91109, USA, 135 pp.

[27] Geosoft 2014: Oasis Montaj Gridding (p. 21). Toronto: Geosoft Oasis Montaj.

[28] Vincent, R.K., 1997: Fundamentals of Geological and Environmental Remote Sensing: Upper Saddle River, NJ: Prentice-Hall, Inc.

[29] Perry, J., Vincent, R., 2009: ASTER brightness and ratio codes for minerals: Application to lithologic mapping in the West Central Powder River Basin, Wyoming. Society of Exploration Geologists. Reviews in Economic Geology 16, 143-168.

[30] Loughlin, W.P., 1991: Principal Component Analysis for alteration mapping. Photogrammetric Engineering and Remote Sensing 57, 1163-1169.

[31] Ruiz-Armenta, J.R., Prol-Ledesma, R.M., 1998: Techniques for enhancing the spectral response of hydrothermal alteration minerals in Thematic Mapper images of Central Mexico. International Journal of Remote Sensing 19, 1981-2000.

[32] Tangestani, M.H., Moore, F., 2002: Porphyry copper alteration mapping at the Meiduk area, Iran. International Journal of Remote Sensing 23, 4815-4826.

[33] Carranza, E.J.M., Hale, M., 2002: Mineral imaging with Landsat Thematic Mapper data for hydrothermal alteration mapping in heavily vegetated terrane. International Journal of Remote Sensing 23, 4827 - 4852.

[34] Crosta, A.P., Souza Filho, C.R., Azevedo, F., Brodie, C., 2003: Targeting key alteration minerals in epithermal deposits in Patagonia, Argentina, using ASTER imagery and principal component analysis. Int. J. Remote Sens. 23, 4233-4240.

[35] Farrand, W.H., Harsanyi, J.C., 1997: Mapping the distribution of mine tailings in the Coeur d'Alene River Valley, Idaho, through the use of a constrained energy minimization technique. Remote Sens. Environ. 59 (1), 64–76.

[36] Resmini, R.G., Kappus, M.E., Aldrich, W.S., Harsanyi, J.C., Anderson, M., 1997: Mineral mapping with hyperspectral digital imagery collection experiment (HYDICE) sensor data at Cuprite, Nevada, USA. Int. J. Remote. Sens. 18 (7), 1553–1570.

[37] Abdel-Rahman, A. M. et al. The geochemistry, origin, and hydrothermal alteration mapping associated with the gold-bearing quartz veins at Hamash district, South Eastern desert, Egypt. Sci. Rep. 13, 15058. https://doi.org/10.1038/s41598-023-42313-9 (2023).

[38] Chavez, P. S., Guptill, S. C., & Bowell, J. A. Image processing techniques for thematic mapper data. Proc. ASPRS-ACSM Tech. Paper, 2, pp. 728–742 (1984).

[39] Cengiz, O., Sener, E. & Yagmurlu, F. A satellite image approach to the study of lineaments, circular structures and regional geology in the Golcuk crater district and its environs (Isparta, SW Turkey). J. Asian Earth Sci. 27, 155–163 (2006).

[40] Beaudemin, M. & Fung, K. B. On statistical band selection for image visualization. Photogrammetric Eng. Remote Sens. 67(5), 571–574 (2001).

[41] Hegab, M. A., Remote Sensing & Gamma-Ray Spectrometry Based Gold Related Alteration Zones Detection. Case study (Um Balad area), North Eastern desert, Egypt. Pure Appl. Geophys. 178, 3909–3931. https://doi.org/10.1007/s00024-021-02865-1(2021).

[42] Darnley, A. G. 1973: Airborne gamma-ray techniques-present and future, In uranium exploration methods. International Atomic Energy Agency (IAEA), Proc. of a Panel, Vienna, Austria, 1972, pp. 67-108.

[43] Mahmoud, S., Hegab, M. A. E. R., & Soliman, N. Environmental Impacts of Mining Activities in Um Balad—El Urf Region; Central Eastern Desert. In: Gad, A.A., Elfiky, D., Negm, A., Elbeih, S. (eds) Applications of Remote Sensing and GIS Based on an Innovative Vision. ICRSSSA 2022. Springer Proceedings in Earth and Environmental Sciences. Springer, Cham (2023). https://doi.org/10.1007/978-3-031-40447-4_7.

[44] Hegab, M. A., Abou El Magd, I., & Wahid, A. E. K.H. Revealing Potential Mineralization Zones Utilizing Landsat-9, ASTER and Airborne Radiometric Data at Elkharaza-Dara Area, North Eastern desert, Egypt, the Egyptian journal of remote sensing and space sciences, 27, Issue 4, Pages 716–733, ISSN 1110–9823. (2024). https://doi.org/10.1016/j.ejrs.2024.10.005.

[45] Gemail, K., Abd-El Rahman, N. M., Ghiath, B. M. & Aziz, R. N. Integration of ASTER and airborne geophysical data for mineral exploration and environmental mapping: a case study, Gabal Dara, North Eastern desert, Egypt. Environ. Earth Sci. 75, 592. https://doi.org/10.1007/s12665-016-5368-0 (2016).

[46] Ghoneim, S. M. et al. Application of remote sensing techniques to identify iron ore deposits in the Central Eastern Desert, Egypt: A case study at Wadi Karim and Gabal El-Hadid areas. Arab. J. Geosci. 15, 1596. https://doi.org/10.1007/s12517-022-10871-3(2022).

[47] Green, A.A., Berman, M., Switzer, P., Craig, M.D., 1988: A transformation for ordering multispectral data in terms of image quality with implications for noise removal. IEEE Trans. Geos. Remote Sens. 26(1), 65-74.

[48] Boardman, J.W., Green, R.O., 2000: Exploring the spectral variability of the earth as measured by AVIRIS in 1999, in: Summaries of the Ninth annual JPL Airborne Geosciences Workshop. Jet Propulsion Laboratory Special Publication 18, 10.

[49] Darnley, A. G. 1973: Uranium prospecting using geochemical and radiometric techniques. Geological Survey of Canada, Economic Geology Report 31.

[50] Boyle, R. W. 1982: Geochemical prospecting for thorium and uranium deposits. Elsevier.

[51] Grasty, R. L., & Cox, J. R. 1997: A review of gamma-ray spectrometric data processing techniques for the determination of uranium concentration in the ground. Journal of Geochemical Exploration, 60(2), 161–176. https://doi.org/10.1016/S0375-6742(97)00033-8.

[52] International Atomic Energy Agency (IAEA), 2003: Guidelines for Radioelement Mapping Using Gamma-ray Spectrometry Data, Technical Reports Series No., IAEA-TECDOC-1363, Vienna, Austria, 179 p.

[53] International Atomic Energy Agency (IAEA), 2005: Decommissioning of Nuclear Facilities, IAEA safety standard series, 27 p.

[54] International Atomic Energy Agency (IAEA), 2010: Quantitative Analysis of Radioelement Data from Natural Sources. International Atomic Energy Agency, IAEA-TECDOC-1613. Vienna, Austria.

[55] Wilford, J. R. 2012: A Weathering Intensity Index for the Australian Continent Using Airborne Gamma-ray Spectrometry and Digital Terrain Analysis. Geoscience Australia, Record 2012/29. Canberra: Geoscience Australia.

[56] Efimov, M. D. 1978: Radiogeochemistry. Nedra Publishing, Moscow.

[57] Drew, L. J., Schuenemeyer, J. H., & Sutphin, D. M. 2013: Uranium Deposits in Magmatic and Metamorphic Rocks—An Assessment of Favorability. USGS Scientific Investigations Report 2012–5577.

[58] Neveen S Abed, Mohamed G El Feky, Atef El-Taher, Ehab El Sayed Massoud, Mahmoud R Khattab, Mohammed S Alqahtani, El Sayed Yousef, Mohamed Y Hanfi 2022 Geochemical Conditions and Factors Controlling the Distribution of Major, Trace, and Rare Elements in Sul Hamed Granitic Rocks, Southeastern Desert, Egypt. Minerals 12 (10), 1245.

[59] Oraby, AH., Saleh, GM., Hassan, EM., Eldabour, SE., El Tohamy, AM., Kamar, MS., El Feky, MG., El Taher, A 2022 Natural Radioactivity and Radioelement Potentiality of Mylonite Rocks in Nugrus Area, Southeastern Desert, Egypt. Radiochemistry 64 (5), 645-655.